Infiltration through porous media

W. Hwang and S. Redner
Center for BioDynamics, Center for Polymer Studies, and Department of Physics, Boston University, Boston, Massachusetts 02215
(Received 6 September 2000; published 24 January 2001)

We study the kinetics of *infiltration* in which contaminant particles, which are suspended in a flowing carrier fluid, penetrate a porous medium. The progress of the ''invader'' particles is impeded by their trapping on active ''defender'' sites which are on the surfaces of the medium. As the defenders are used up, the invader penetrates further and ultimately breaks through. We study this process in the regime where the particles are much smaller than the pores so that the permeability change due to trapping is negligible. We develop a family of microscopic models of increasing realism to determine the propagation velocity of the invasion front, as well as the shapes of the invader and defender profiles. The predictions of our model agree qualitatively with experimental results on breakthrough times and the time dependence of the invader concentration at the output. Our results also provide practical guidelines for improving the design of deep bed filters in which infiltration is the primary separation mechanism.

DOI: 10.1103/PhysRevE.63.021508 PACS number(s): 83.80.Hj, 47.55.Kf, 47.55.Mh

I. INTRODUCTION

In depth filtration, suspended particles in a fluid are removed during their passage through a porous medium [1,2]. The basic dynamics of depth filtration is determined primarily by the pore structure of the filter, the particle size distribution, and various physicochemical and hydrodynamic details. If the particle size is larger than the typical pore size, particles get stuck relatively quickly. The permeability of the filter decreases steadily during this process and drops to zero when clogging is reached. This process is often referred to as sieving or straining [3]. Conversely, if particles are much smaller than the pore size and if particles are trapped only at the interfaces of the porous medium, the flow field is only slightly affected by the trapping. The goal of this paper is to provide a general understanding of this latter process of *infiltration* by microscopic network modeling.

Infiltration underlies many practical situations, such as underground waste disposal [4], gas mask design, or drinking water filters [5]. Typically, submicrometer size contaminant particles are suspended in a carrier fluid and flow through a porous material, such as a sand filter whose typical grain size is much larger than the contaminant particles, or an ion exchange filter [5] where the contaminant size is molecular in scale. In such cases, one can neglect the change of the flow field due to particle trapping [4], an approximation that considerably simplifies theoretical analysis.

The kinetics of infiltration is controlled by the microscopic mechanisms for the trapping of the invader particles. Typically each pore can hold a limited number of particles due to a finite surface area or a finite range of the surface potential. When all the available surface area is covered by particles, subsequent invaders flow passively through the filter without being trapped (see Fig. 1). Our basic goal is to understand the kinetics of this infiltration and the ultimate breakthrough of the invader, as well as the evolution of the invader and defender density profiles as functions of downstream position and time.

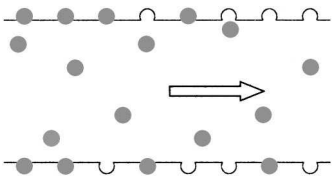

FIG. 1. Idealized picture of infiltration. Suspended particles are trapped at ''defender'' sites on pore surfaces. Once defenders are occupied, subsequent particles pass by freely.

Previous work on infiltration in porous media has often been based on a macroscopic convection-diffusion equation description, with reaction terms introduced to account for particle trapping [4,6,7]. Another approach has been to use a single absorbing sphere to calculate the collection efficiency at the initial stage of filtration [8]. While numerical simulations of these models have some predictive power, it is hard to develop a connection between this macroscopic approach and basic features of the microscopic process, such as the concentration profiles of the trapped and flowing particles.

For filtration by straining, models based on a discrete network description of the filter medium are relatively well developed [9–13]. To our knowledge, however, there has been no microscopic network modeling work on infiltration. As in the case of straining, a spatial density gradient naturally arises in infiltration, since particles begin to deposit at the upstream end of the filter and advance downstream as the filter gets used up. The density gradient is experimentally observed as the time-dependent output concentration [6]. In this paper, we will account for this basic experimental observation by using a discrete network approach.

Practical questions raised by infiltration are the breakthrough time, which is defined as the time for the output concentration to reach a specified threshold level, and the filter efficiency, which is related to the fraction of the filter material actually used before breakthrough. Clearly, it is desirable to use as much of the filter material as possible before breakthrough occurs.

This paper is organized as follows. In Sec. II, we introduce the basic parameters that govern particle trapping and provide a qualitative picture of infiltration. In the following sections, we construct a sequence of discrete models with

 ©2001 The American Physical Society

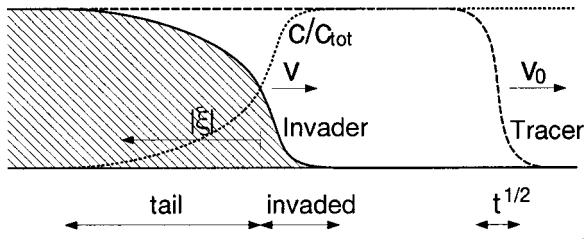

FIG. 2. Infiltration profiles. Horizontal direction is downstream. The invader density profile (shaded) is exponential in the invaded region, while the capacity profile has a power law tail, $c \sim |\xi|^{-\lambda}$.

increasing complexity and realism to ultimately provide a lattice network description. In Sec. III, we discuss the case of a one-dimensional (1D) chain of trapping sites and, in Sec. IV, we analyze infiltration in the bubble model to provide a mean-field-like description. Building on these results, we then turn to simulations of infiltration on tube lattice networks in Sec. V. We summarize and compare our results with experiments in Sec. VI.

II. BASIC PICTURE

The two basic characteristics of particle trapping are the efficiency of an unoccupied trapping site and the number of trapping sites in a pore. We introduce the trapping probability γ as the probability that a particle is trapped upon encountering an open collector site. The parameter γ thus represents the strength of the particle-collector interaction and accounts for the possibility that contact between particles and the filter grains may not necessarily lead to deposition [14]. While this simplifies the complicated adsorption mechanism, later we show that basic features like the invasion front propagation velocity (Fig. 2) is independent of the interaction details.

Next we introduce the capacity $c_x(t)$ as the number of particles a pore at position x can hold at time t. In the case of noncoagulating particles, which cannot get trapped on top of an already adsorbed particle, the initial capacity is proportional to the inner surface area of the pore and then decreases as the pore surface is covered by particles. For simplicity, we ignore multiple trapping on an already occupied collector site as well as particle relaunching. The key factors that determine the dynamic behavior of the system are geometric, such as the capacity of a clean filter and the pore size distribution, and kinematic, such as the particle concentration and the flow rate. More refined models for particle trapping can be incorporated within our basic modeling.

Consider a generic infiltration process based on the above concepts. Initially a layer in the clean filter has a total capacity $c_{\rm tot}$ independent of the downstream position. At $t=0$, a fluid that contains a mixture of invader and nonreacting tracer particles enters the filter whose flow rate is determined by the steady-state solution of d'Arcy's law. Tracer particles passively follow the fluid motion and advance with the average flow velocity v_0. The width of the tracer density profile spreads as $t^{1/2}$ due to hydrodynamic dispersion (Fig. 2). Invader particles first encounter clean collector sites. Because each such encounter leads to deposition with probability γ, the survival probability of the particles in this leading invaded region decreases exponentially with downstream position as illustrated in Fig. 2. As particles advance and get trapped, the pore capacity decreases and subsequent particles are more likely to survive, giving rise to an advancing invasion front with a velocity $v<v_0$. In principle, the propagation velocity and shape of the front are functions of time. However, at long times these features approach steady-state values. Another important feature is that the trailing edge of the capacity profile decays as a power of the distance $|\xi|$ ($\xi<0$) from the invasion front whose location is defined, e.g., as the position where $c=c_{\rm tot}/2$. For large $|\xi|$, any reasonable definition for the front location can be used.

The existence of different propagation velocities v_0 for the pure fluid and $v<v_0$ for the contaminant leads to purification of the liquid. The filter can be used until the invaded region reaches the outlet end. For a filter of length L, the breakthrough time will be of the order of L/v, so the amount of throughput will be approximately proportional to Lv_0/v.

III. ONE-DIMENSIONAL MODEL

As a preliminary, we study infiltration in a one-dimensional chain of identical pores at $k=0,1,2,\ldots$. First we consider the case where each pore can accommodate only one particle and then we generalize to multiple capacity pores.

A. Single capacity pores

We choose a time unit such that one particle is injected at each discrete time step. Multiple particle injection leads to a different particle density and will affect only the overall scale factor but not change qualitative features of the system. The carrier fluid advances by one pore distance at each time step; that is, its velocity is unity. When particle trapping occurs in a pore at k, the capacity $c_k(t)$ changes permanently from 1 to 0. At time t, a particle at pore k gets trapped in that pore with probability γ if $c_k(t)=1$. A particle advances to the next pore in one time step with probability 1 if $c_k(t)=0$. Based on these elemental steps, we introduce the following two probability densities: (i) $p_k(t)$, the probability that a freely moving particle is in pore k at time t; (ii) $q_k(t)$, the probability that the pore at site k is unoccupied, that is, $c_k(t)=1$. The corresponding master equations for $p_k(t)$ and $q_k(t)$ are

$$p_k(t+1)=p_{k-1}(1-\gamma q_{k-1}), \tag{1}$$

$$q_k(t+1)=q_k(1-\gamma p_k), \tag{2}$$

where we drop the argument t on the right hand side for simplicity. Unless there is a possibility for confusion, we will not write the argument t in related formulas. Since a particle advances to the next pore in one time step, $p_k(t+1)$ depends on $p_{k-1}(t)$. The term $(1-\gamma q_{k-1})$ in Eq. (1) is the probability that the particle at $k-1$ does not get trapped by an unoccupied pore also at $k-1$. Similarly, the term $(1-\gamma p_k)$ in

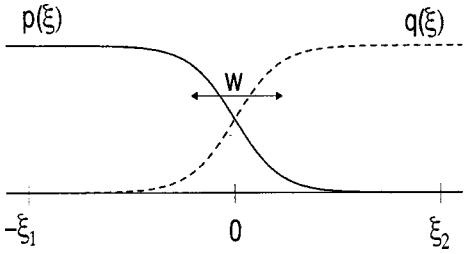

FIG. 3. Steady-state profile in the single capacity model.

Eq. (2) is the probability that pore k does not trap a free particle at time t. The initial and boundary conditions for these equations are

$$p_{k\geqslant 1}(0)=0, \quad q_k(0)=1; \quad p_0(t)=1, \quad q_\infty(t)=1. \tag{3}$$

If the trapping probability γ is small, a particle can advance many pores without being trapped, so that $p_k(t)$ and $q_k(t)$ vary slowly in space and time and a continuum approximation can be applied. Letting $k+1\to x+\delta x$ and $t+1\to t+\delta t$, Eqs. (1) and (2) become, to lowest order,

$$\begin{aligned} \partial_t p + v_0 \partial_x p &= -\gamma pq, \\ \partial_t q &= -\gamma pq, \end{aligned} \tag{4}$$

where $v_0 \equiv \delta x/\delta t = 1$, and $\gamma \to \gamma/\delta t$ is a redefinition of the trapping probability in units of the infinitesimal time increment.

In a comoving reference frame $\xi \equiv x - vt$, with v the invasion front propagation velocity shown in Fig. 2 (which is yet to be determined), Eqs. (4) become

$$(v_0 - v)\partial_\xi p + \partial_t p = -\gamma pq, \tag{5}$$

$$-v\partial_\xi q + \partial_t q = -\gamma pq. \tag{6}$$

Let us first examine the steady-state solution of Eqs. (5) and (6). Setting the time derivatives to zero, subtracting Eq. (6) from Eq. (5), and integrating with respect to ξ gives

$$(v_0 - v)p(\xi) + v q(\xi) = \text{const}. \tag{7}$$

The integration constant can be determined by applying Eqs. (3) in the comoving frame. As $\xi \to -\infty$, $p \to 1$, $q \to 0$, and as $\xi \to \infty$, $p \to 0$, $q \to 1$. These immediately give $v = v_0/2 = 0.5$. Note that v is determined entirely from the boundary condition (and v_0) in the comoving frame, and not from the interaction strength γ. This feature continues to hold for all the models in this paper.

Using Eq. (7) with $v = v_0/2$, Eqs. (5) and (6) can be solved to give

$$p(\xi) = \frac{1}{1+e^{\xi/\xi_0}}, \quad q(\xi) = \frac{1}{1+e^{-\xi/\xi_0}} \tag{8}$$

(Fig. 3). Thus $\xi_0 \equiv v_0/2\gamma$ is the characteristic width w of the profile. Notice also that the profiles of p and q are symmetric about their intersection. We verified both the dependence of the width on γ and the profile shape predicted by Eq. (8) by numerical integration of the master equations (1) and (2).

One subtle point is the rate of approach to the steady state. First, we find that the asymptotic propagation velocity $v = v_0/2$ is reached before the asymptotic profile is established. This arises because v is determined by the boundary conditions, and not by interaction details. We also verified this feature numerically. Adopting this asymptotic velocity, Eqs. (5) and (6) are then symmetric in p and q. In fact, the system is identical to two-species annihilation, $A + B \to 0$, where each species is ballistically injected from opposite sides with velocity $+v_0/2$ for the A's and $-v_0/2$ for the B's.

Thus most of the time variation in Fig. 3 occurs in the reactive region of width w, where $w = 0$ at $t = 0$. Integrating Eq. (5) from $-\xi_1 \ll 0$ to $\xi_2 \gg 0$ gives

$$-\frac{v_0}{2} + \partial_t \int_{-\xi_1}^{\xi_2} p\, d\xi = -\gamma \int_{-\xi_1}^{\xi_2} pq\, d\xi. \tag{9}$$

The integral on the left hand side is the area under the curve $p(\xi)$ between $-\xi_1$ and ξ_2, whose time dependence mainly comes from the change in w. On the right hand side, the integral is approximately proportional to w, since pq is significantly different from zero only in the reactive region. We can then rewrite Eq. (9) as

$$-\frac{v_0}{2} + c_1 \partial_t w \simeq -\gamma c_2 w, \tag{10}$$

where c_1 and c_2 are constants. Integrating Eq. (10) and applying the condition $w(\infty) \sim v_0/2\gamma$ gives an exponential decay to the steady state $w(t) \sim (v_0/2\gamma)(1 - e^{-c_2 \gamma t})$.

It is worth emphasizing that the symmetry between the invader and defender is generally responsible for the relation $v = v_0/2$. At the inlet, invaders are injected with velocity v_0, and the invasion front advances with velocity v, with one invader particle annihilating with one defender site. In the reference frame moving with velocity v_0, the situation is reversed. The invaders are at rest and defenders are injected with velocity v_0 from the opposite direction. Therefore the invasion front advances with velocity $v_0 - v$. Since these two reference frames describe the system in the same way, the front velocities should be the same; that is, $v = v_0 - v$, or $v = v_0/2$.

B. Multiple capacity pores

Now we consider the case where each pore can trap M particles, that is, the initial pore capacity is $c_k(0) = M$. We again follow the previous rules of injecting a single particle and advancing a particle by one pore ($v_0 = 1$) at each time step. Multiple particle injection or different injection intervals again simply change the overall concentration and time scale.

In a multiple capacity pore, the probability of encountering an open trap in a pore needs to be considered, in addition to the trapping probability γ upon encounter with an open trap. Generally, the encounter probability decreases as more particles get trapped, since the inner pore surface area avail-

able for trapping shrinks. When fluid mixing within a pore is weak, a particle can encounter only one trap, either open or occupied. Then the encounter probability is approximately proportional to the fraction of the open surface area. On the other hand, if the mixing is perfect, a particle encounters all the available traps in a pore before exiting.

For practically relevant situations, pores are sufficiently short so that a particle in a pore follows streamlines without transverse diffusive mixing [15]. In what follows, we consider this limit of weak mixing. For a pore with n out of M traps available, the encounter probability is n/M, and the overall trapping probability of this pore is $T_n \equiv \gamma n/M$. In writing this expression, we ignore the possibility that a particle far from the pore wall does not encounter any traps. In Sec. VI, we argue that this volumetric effect does not change the basic behavior of infiltration.

To describe the evolution of the system, we use the same single particle probability density $p_k(t)$ as in the single capacity pore system, but modify the probability density for the capacity as follows: $q_k^n(t)$ is the probability that a pore at position k contains n open traps. This is the same as the probability that $c_k(t)=n$, for $0 \leqslant n \leqslant M$. Following similar reasoning as that applied to deduce Eqs. (1) and (2), the master equations for $p_k(t)$ and $q_k^n(t)$ are

$$p_k(t+1)=p_{k-1}\left[q_{k-1}^0+\sum_{n=1}^{M} q_{k-1}^n(1-T_n)\right], \qquad (11)$$

$$q_k^n(t+1)=q_k^n(1-p_kT_n)+p_kq_k^{n+1}T_{n+1}. \qquad (12)$$

In Eq. (11), $q_{k-1}^0(t)$ accounts for the case that the pore $k-1$ has zero capacity. Other terms in Eq. (11) correspond to cases when the capacity is different from 0, with $(1-T_n)$ the survival probability for each case. In Eq. (12) $q_k^n(1-p_kT_n)$ is the probability that the pore with capacity n does not trap a particle, and $p_kq_k^{n+1}T_{n+1}$ is the probability that the capacity decreases from $n+1$ to n by a particle trapping event. Hence the last term is absent when $n=M$.

We simplify Eqs. (11) and (12) by introducing the *average capacity* of a pore at position k,

$$Q_k(t) \equiv \sum_{n=1}^{M} nq_k^n(t). \qquad (13)$$

This gives the average number of sites still available for trapping in the pore. Now by multiplying Eq. (12) by n, summing from 1 to M, and using $\Sigma_{n=1}^{M} q_k^n(t)=1-q_k^0(t)$, we obtain

$$p_k(t+1)=p_{k-1}\left(1-\frac{\gamma}{M}Q_{k-1}\right), \qquad (14)$$

$$Q_k(t+1)=Q_k\left(1-\frac{\gamma}{M}p_k\right). \qquad (15)$$

These are identical in form to Eqs. (1) and (2), so the same steady-state analysis applies. We transform to a comoving frame and take the continuum approximation to reduce the rate equations to Eqs. (5) and (6) with $\gamma \to \gamma/M$ and $q \to Q$. The boundary conditions are also the same as in the case of single capacity pores, except $Q(\xi \to \infty)=M$. Combining these results gives

$$v=\frac{v_0}{1+M}, \quad w(\infty) \sim \frac{v_0M}{\gamma(1+M)}. \qquad (16)$$

Notice that for $M=1$ Eq. (16) reduces to the single capacity case, while for $M \to \infty$, $v \to 0$. This means that there is no steady state for the case of infinite capacity pores.

We can generalize the symmetry argument given in the single capacity case to find the propagation velocity in Eq. (16). At the input, the flux of invaders moving with the carrier fluid is equal to $1 \times v_0$. Similarly, in the reference frame moving with velocity v_0, the flux of defenders is $M \times v_0$, while the invaders are at rest. Because one invader annihilates with one defender, the two particles are kinetically indistinguishable. Therefore, if a particle flux of $1 \times v_0$ results in a front moving with velocity v, the front velocity produced by a flux of $M \times v_0$ should be Mv, which, in turn, equals v_0-v in the moving reference frame. By this equivalence, Eq. (16) immediately follows.

In the limit of perfect mixing, a particle encounters all traps in the pore. The overall trapping probability with n open traps is then $T_n=1-(1-\gamma)^n$. In the limit of small γ, $T_n \simeq \gamma n$; thus the analysis is exactly the same as in the poor mixing case except without the factor $1/M$ in T_n. The propagation velocity of the front is the same as in Eq. (16), since this velocity is independent of trapping mechanism, while the width varies as $w \sim v_0/\gamma(1+M)$. Notice that w is a decreasing function of M. This arises because a particle must survive all the traps in a pore before advancing to the next pore. Finally, for a mixing mechanism that is intermediate between the two limits of perfect and poor mixing, the propagation velocity will be $v_0/(1+M)$, while the width of the front will lie between the limiting values of $v_0/\gamma(1+M)$ and $v_0M/\gamma(1+M)$.

IV. THE BUBBLE MODEL

We now study the bubble model as a logical next step toward understanding infiltration in porous media. The bubble model was introduced to account for the breaking of fibers [16], extremal voltages in resistor networks [17], and later filtration kinetics [11]. The bubble model consists of L ''bubbles'' in series, each of which is a parallel bundle of w tubes, with each tube representing a pore (Fig. 4). A bubble can be viewed as a single layer of parallel bonds in a lattice with all the ends ''shorted.'' This model has multiple paths, as in real porous media, and is sufficiently simple to be

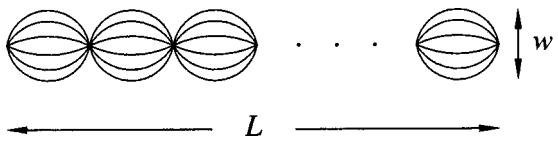

FIG. 4. The bubble model consists of L bubbles connected in series, each bubble with w tubes.

amenable to analytic study. A useful feature of the bubble model is that for straining dominated filtration this model predicts similar behavior to that of lattice networks [11].

We choose the tube radii in the bubble model from the Hertz distribution

$$f(r)=2\alpha r e^{-\alpha r^2}, \tag{17}$$

where $\alpha^{-1/2}$ is the characteristic pore radius. This form is often seen in experimental pore size measurements [18] and has been used for modeling the pore size distribution in filters [3,11]. For simplicity we assume identical tube lengths and measure downstream distance in units of the tube length, which is set equal to 1. We also assume that the flow rate in a tube of radius r is proportional to $-r^{\mu}\nabla P$, where ∇P is the pressure gradient along the tube and μ depends on the nature of the flow, with $\mu=4$ corresponding to Poiseuille flow and $\mu=2$ to Euler flow. Perfect mixing is assumed at each node. A particle chooses a tube in the next downstream bubble according to the *flow induced probability* $\Phi(r)$,

$$\Phi(r)=\frac{r^{\mu}}{\int dr'\, f(r')r'^{\mu}}, \tag{18}$$

in which the probability of choosing an outgoing tube of radius r is proportional to the flow rate into the tube, r^{μ} [11,13].

Since tubes of different flow velocities give the dominant mechanism for dispersion, the radial dependence of the local flow velocity in a tube (Taylor dispersion) is ignored. Thus we assume that a particle moves with the average flow velocity $v(r)$ along the tube. We now investigate the hydrodynamic dispersion of passive Brownian particles which are carried by the background fluid in the bubble model, in the absence of any trapping. This will provide the concepts and tools necessary to understand infiltration in the bubble model.

A. Hydrodynamic dispersion in the bubble model

In the large w limit, each bubble is nearly identical, and we can regard the particle motion as a directed random walk in which the average residence time τ_k in bubble k ($k=0,1,2,\ldots$) is a random variable whose distribution $R(\tau)$ is related to the flow induced entrance probability $\Phi(r)$ and the radius distribution $f(r)$. This random walk description of the continuous particle motion introduces an additional stochasticity into the system. However, we will show below that this only modifies the hydrodynamic dispersion coefficient by an overall multiplicative factor.

The master equations for $p_k(t)$, the probability that there is a particle in the kth bubble at time t, are

$$\frac{dp_0}{dt}=\rho\phi-\frac{p_0}{\tau_0}, \quad \frac{dp_k}{dt}=\frac{p_{k-1}}{\tau_{k-1}}-\frac{p_k}{\tau_k}. \tag{19}$$

Here ρ is the initial particle number concentration, ϕ is the (constant) flow rate, and the initial condition is $p_k(0)=0$ for all k. Since the flow rate does not change in infiltration, constant pressure drop and constant flow rate conditions are equivalent.

The particle transport properties can be obtained in terms of the residence time distribution $R(\tau)$, namely, the probability that a particle spends a time τ in a bubble. This residence time distribution is related to microscopic distributions by

$$R(\tau)=\int_0^{\infty} dr\,\Phi(r)f(r)\delta\left(\tau-\frac{1}{v(r)}\right), \tag{20}$$

where $\delta(x)$ is the Dirac delta function. Since the flow rate into a tube of radius r is $\phi\Phi(r)$, the average flow velocity $v(r)=\phi\Phi(r)/\pi r^2$. Using this together with Eq. (17) for $f(r)$, we obtain the first two moments of τ,

$$\langle\tau\rangle=\int_0^{\infty}\tau' R(\tau')d\tau'=\frac{\pi}{\phi\alpha}\equiv\frac{V}{\phi}, \tag{21}$$

$$\langle\tau^2\rangle=\langle\tau\rangle^2\Gamma\left(1+\frac{\mu}{2}\right)\Gamma\left(3-\frac{\mu}{2}\right), \tag{22}$$

where $V=\langle\pi r^2\rangle$ is the average tube volume (recall that the tube length is fixed to be 1) and $\Gamma(x)$ is the gamma function.

We solve Eq. (19) in the Appendix by the Laplace transform technique. From this solution, the average propagation velocity and the width of the front are

$$v_0\simeq\frac{1}{\langle\tau\rangle}, \tag{23}$$

$$w\simeq\left\{\frac{t}{\langle\tau\rangle}\left[2\Gamma\left(1+\frac{\mu}{2}\right)\Gamma\left(3-\frac{\mu}{2}\right)-1\right]\right\}^{1/2}\equiv(D_{\parallel}t)^{1/2}. \tag{24}$$

Thus we see that the dispersion coefficient is proportional to the average flow velocity $\langle\tau\rangle^{-1}$. When $\mu=2$ (Euler flow), the flow velocities in all the tubes are identical and there should be no dispersion. However, Eq. (24) gives a nonzero dispersion coefficient. As mentioned above, this arises from the stochasticity of the random walk picture for the particle motion. For the practically relevant case of $\mu\simeq4$, the effect of this stochasticity is only to change the dispersion coefficient by a factor of order unity.

B. Infiltration in the bubble model

To describe infiltration in the bubble model, we need to specify the particle motion, the tube capacities, and particle trapping in a tube. For the particle motion we again assume that a particle chooses a tube according to flow induced probability and then advances with the average flow velocity $v(r)$ of this tube. The capacity of a tube is proportional to its inner surface area, which is proportional to the tube radius, since all tubes have the same length. Last, the overall trapping probability of a tube is equal to the microscopic trapping probability γ multiplied by the fraction of open traps in a tube (Sec. III B).

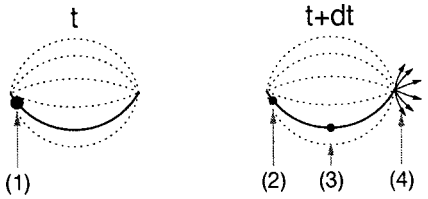

FIG. 5. Propagation of the PDF in tube β at bubble k. (1) Initial probability element $p_k^\beta(t)$. (2) Fraction remaining. (3) Fraction trapped. (4) Fraction advancing. This last element enters the next bubble and is then immediately split among the tubes according to the flow induced probabilities.

To simulate this process efficiently we propagate the probability distribution function (PDF) of the suspended particles rather than simulating the motion of individual particles [19,20]. The PDF propagation therefore provides the exact distribution of particle positions and tube capacities for a single realization of tube radii. Conceptually, the PDF algorithm is equivalent to an exact integration of the master equations.

To implement the PDF propagation, we define $p_k^\beta(t)$, the probability that there is a particle at the *entrance* of tube β in bubble k ($\beta=1,2,\ldots,w$, $k=0,1,2,\ldots$); $c_k^\beta(t)$, the capacity of tube β in bubble k. Since particles generally have different velocities, their positions could be anywhere within a tube. We simplify this by forcing particles to *always* be at the tube entrance by adjusting the time unit and the PDF propagation so that the *average* particle position is at the correct location along the tube, as illustrated in Fig. 5.

To construct the particle motion, let us temporarily disregard particle trapping. We set the time increment to be $\delta t = 1/v_{\max}$, where $v_{\max}$ is the maximum flow velocity among all tubes. In a time δt, a particle at the entrance of the fastest tube should traverse the entire tube length, which is equal to 1. We then let a particle in a slower tube, with velocity $v_k^\beta < v_{\max}$, travel a distance 1 with probability $u_k^\beta \equiv v_k^\beta/v_{\max}$, or remain fixed with probability $1-u_k^\beta$. One can regard u_k^β as a normalized flow velocity. By construction, such a particle travels the correct average distance in time δt, $1\times u_k^\beta + 0\times(1-u_k^\beta) = v_k^\beta/v_{\max} = v_k^\beta \delta t$.

Let us now recast this random walk into a probability propagation algorithm. Consider an element of the PDF that is at the junction before the kth bubble. Before any particle motion occurs, we split this probability element among the downstream bonds in this bubble according to the flow induced probability at the tube entrance. We can view the probability element as advancing infinitesimally into each bond, as indicated on the left side of Fig. 5. Once this initial tube assignment is made, the probability element remains within its assigned tube until it reaches the next junction.

Now consider the motion of a probability element that has just entered a particular bond. After a time δt, a fraction u_k^β of the PDF is advanced to the next bubble, while a fraction $1-u_k^\beta$ remains fixed at the entrance to bond β.

Due to the filtration, a fraction of the flowing PDF becomes trapped in tube β in the kth bubble at a rate that is proportional to the tube capacity $c_k^\beta(t)$. The overall trapping probability of this tube is therefore $T_k^\beta = \gamma c_k^\beta(t)/c_k^\beta(0)$. After trapping has occurred, the tube capacity is decremented according to the following prescription. When one unit of PDF (equivalent to one particle) gets trapped, we define the bond capacity to be decreased by Δ. Therefore Δ is just the surface area covered by one particle. Correspondingly, $c_k^\beta(0)/\Delta$ equals the number of particles the tube can accommodate.

Our algorithm for propagating an element of probability at the entrance to bond β in the kth bubble over a time δt therefore consists of the following steps (Fig. 5):

(1) The fraction of PDF remaining at the start:
$$p_k^\beta(1-u_k^\beta).$$
(2) The fraction trapped in tube β:
$$p_k^\beta u_k^\beta T_k^\beta.$$
(3) The fraction advancing to the next junction:
$$p_k^\beta u_k^\beta(1-T_k^\beta).$$
(4) The capacity change of the tube by trapping:
$$-\Delta\times[p_k^\beta u_k^\beta T_k^\beta].$$

The rate equations that account for these steps are

$$p_k^\beta(t+\delta t) = p_k^\beta(1-u_k^\beta) + \Phi_k^\beta \sum_{\beta'=1}^{w} p_{k-1}^{\beta'} u_{k-1}^{\beta'}(1-T_{k-1}^{\beta'}), \tag{25}$$

$$c_k^\beta(t+\delta t) = c_k^\beta - \Delta p_k^\beta u_k^\beta T_k^\beta. \tag{26}$$

The first term on the right hand side of Eq. (25) is the fraction of probability that does not move, and the second term is the contribution from elements of probability that has moved from the previous site. The flow induced probability Φ_k^β in Eq. (25) accounts for the fraction of PDF that enters into tube β.

To test this approach, we set $\gamma=0$ (no trapping) in the above rate equations and simulate the PDF propagation. By this method, we find a traveling front whose basic properties coincide with the hydrodynamic dispersion results given by Eqs. (23) and (24).

It is also worth mentioning that our PDF algorithm can be generalized to allow for hopping a distance that is a fraction of the tube length. In this manner one can account for different longitudinal flow velocities at different radial positions within a tube (Taylor dispersion [7]). In the limit of an infinitesimal hopping distance, continuous particle motion is reproduced by the PDF algorithm. Unfortunately, the gain in having a more accurate description of the motion is offset by the complexity of the algorithm and the large increase in the computation time.

C. Asymptotic behavior

To obtain the average invasion front profile over the tubes in each bubble, we define the bubble-average quantities $P_k(t) \equiv (1/w)\Sigma_\beta p_k^\beta(t)$ and $Q_k(t) \equiv (1/w)\Sigma_\beta c_k^\beta(t)$. We first derive the invasion front velocity via the symmetry argument of Sec. III B. A rigorous derivation of the front velocity from the master equations for $P_k(t)$ and $Q_k(t)$ is given in [21].

The carrier fluid is moving with velocity v_0 [Eq. (23)] and the input flux of invaders per tube is equal to $v_0\rho V$, since ρV is equal to the number of invader particles per tube volume

in the input fluid. On the other hand, in a reference frame moving with velocity v_0, the input flux of defenders is equal to $v_0 M$ where $M \equiv \langle r \rangle / \Delta$ is the average initial number of invaders a tube can accommodate. Following the argument in Sec. III B, we find that the front velocities v and $v_0 - v$ in the two reference frames are related by $Mv = \rho V (v_0 - v)$, yielding

$$\frac{v}{v_0} = \left(1 + \frac{M}{\rho V} \right)^{-1}. \tag{27}$$

Good filter performance means that the breakthrough time is long or, equivalently, that the propagation velocity is slow. Equation (27) implies that the propagation velocity can be made small by increasing the capacity of a pore, or by decreasing either the filter grain size or the input particle concentration. Notice that neither the reaction strength γ nor the nature of the flow [through $v(r) \sim r^{\mu-2}$] affects this propagation velocity.

We now study the asymptotic density profiles. Instead of working directly with the averaged quantities $P_k(t)$ and $Q_k(t)$, we first focus on the behavior of a single tube of radius r, since tubes with the same radius in a bubble have identical time dependence. The asymptotic profiles can be obtained after averaging over the distribution of tube radii. Therefore, we label tubes according to their radii instead of the index β. We denote by $p_k(t;r)$ and $c_k(t;r)$ the PDF and capacity of a tube of radius r in the kth bubble.

Let us first focus on the PDF profile in the invaded region. Here, traps are mostly unoccupied, so that the tube capacity $c_k(t;r)$ is approximately equal to its initial value $c_k(0;r)$, which is proportional to the tube radius, and we set it equal to r. The arbitrariness in the unit of capacity can be controlled by the magnitude of the parameter Δ. Then Eq. (25) becomes

$$p_k(t+\delta t;r) \simeq p_k(t;r)[1-u(r)] + (1-\gamma)\Phi(r) \int dr' f(r') p_{k-1}(t;r') u(r'), \tag{28}$$

where the integration over r' replaces the summation over the tube index. The flow induced probability $\Phi(r)$ and normalized velocity $u(r)$ are independent of the downstream position k because these depend only on the radius of a tube.

The equation for $P(x,t)$ can be obtained by multiplying Eq. (28) by $f(r)$ and integrating over r. As in Sec. III, we take $\gamma \ll 1$ and consider the continuum limit. If we redefine the length of the bubble from 1 to δx, δt becomes $\delta x / v_{\max}$. Integrating Eq. (28) and expanding in δt and δx yields

$$\delta t\, \partial_t P(x,t) = -\int dr f(r) u(r) [\delta x\, \partial_x p(x,t;r) + \gamma p(x,t;r)]. \tag{29}$$

Here, we use $\int dr f(r) \Phi(r) = 1$. Dividing Eq. (29) by δt changes $u(r)$ back to $v(r)$. After redefining $\gamma \to \gamma / \delta x$ as before, we obtain

$$\partial_t P \simeq -\int dr f(r) v(r) [\partial_x p(x,t;r) + \gamma p(x,t;r)]. \tag{30}$$

In the steady-state comoving frame, Eq. (30) becomes

$$v \partial_\xi P \simeq \int dr f(r) v(r) [\partial_\xi p(\xi;r) + \gamma p(\xi;r)]. \tag{31}$$

Since only a small number of particles have entered the invaded region, the density of moving particles is approximately proportional to r^μ, and we introduce the ansatz $p(\xi;r) = r^\mu g(\xi)$ to factorize the PDF. In order to calculate the dominant contribution from the integral in Eq. (31), we substitute $v(r) = v_0 + \delta v(r)$, where $\delta v(r)$ is the deviation from the average carrier fluid velocity v_0. Since $\delta v(r)$ has zero mean, the dominant contribution to the integral over $v(r)$ in Eq. (31) comes from the constant part v_0. Using these approximations in Eq. (31), and using $P(\xi) = \langle r^\mu \rangle g(\xi)$, we find

$$v g' \simeq v_0 (g' + \gamma g). \tag{32}$$

Since $v < v_0$, we find $g(\xi) \sim \exp[-v_0 \gamma \xi / (v_0 - v)]$. Hence the profile of free particles in the invaded region $P(\xi)$ decays exponentially in ξ, with a characteristic decay length that has the same $1/\gamma$ dependence as in the 1D model.

Let us now turn to the analysis of the capacity profile in the tail region. In terms of $p(x,t;r)$ and $c(x,t;r)$, Eq. (26) becomes

$$\partial_t c(x,t;r) = -\Delta \gamma p(x,t;r) v(r) \frac{c(x,t;r)}{r}. \tag{33}$$

Since there is negligible trapping in the tail region, the particle motion follows that of the carrier fluid. Thus $p(\xi;r) \simeq \pi r^2 \rho$, where πr^2 is the tube volume, and the flow velocity is $v(r) = \phi \Phi(r) / \pi r^2 = \phi r^{\mu-2} / \pi \langle r^\mu \rangle$. Substituting these in Eq. (33) and transforming into the comoving frame gives

$$\partial_\xi c(\xi;r) \simeq s r^{\mu-1} c(\xi;r), \tag{34}$$

where $s \equiv \Delta \gamma \rho \phi / v \langle r^\mu \rangle$ denotes the strength of the particle trapping reaction. We now integrate Eq. (34) from $-\xi_1 \ll 0$ to $\xi_2 \approx 0$ and use the boundary condition $c(\xi_2;r) \simeq r$ to obtain

$$c(\xi;r) \simeq r e^{-s r^{\mu-1} |\xi|}, \tag{35}$$

where we drop the subscript of ξ_1.

Finally, the average bond capacity as a function of position with respect to the front, $Q(\xi)$, is

$$Q(\xi) = \int dr f(r) c(\xi;r) \simeq 2\alpha \int dr\, r^2 e^{-s r^{\mu-1} |\xi| - \alpha r^2}. \tag{36}$$

For large $|\xi|$, the integral is dominated by the smallest tubes and the initial distribution of tube radii is irrelevant in the tail region. Hence the factor αr^2 in the exponential can be ignored. Performing the resulting integration gives

$$Q(\xi)\sim\frac{(s|\xi|)^{-3/(\mu-1)}}{(\mu-1)}\Gamma\left(\frac{3}{\mu-1}\right)\propto(\gamma|\xi|)^{-\lambda}, \qquad (37)$$

where the last relation serves to define the *profile exponent* λ. This is one of our primary results. Correspondingly, the PDF in the tail region will approach its initial value with the same power law.

The existence of the power law tail in the capacity profile stems from the fact that the flow rate is not affected by trapping. Thus when large pores are "used up," the fluid still predominantly flows through these pores, leading to a substantial unused capacity in the smaller tubes. It is these unused smaller tubes that contribute substantially to the capacity profile in the tail region. This mechanism is quite general and depends only weakly on the form of the radius distribution. For example, for a uniform distribution in the range $r=(0,1)$, we obtain $\lambda=2/(\mu-1)$. However, if there is a finite lower cutoff in the radius distribution, the PDF will have an asymptotic exponential tail.

It is interesting to note that the density profile has different dependence on γ in the invaded and tail regions. From Eq. (37), the density profile contains an overall factor $\gamma^{-\lambda}$. Thus γ typically does not appear as an overall scale factor of the entire profile, as in the invaded region. However, for the practically relevant case of $\mu=4$, the exponent in Eq. (37) is equal to 1, and γ becomes the overall scale factor of the profile.

D. Numerical results

In our numerical simulations, we set the input particle flux per tube $\rho\phi$ equal to 1, which means that w units of PDF are injected into the system at every time step. This can be achieved by choosing $\rho=1/\pi$ and $\phi=\pi$, which also makes $v_0=\alpha$ [Eqs. (21) and (23)].

We applied the PDF propagation of Eqs. (25) and (26) to a system of size $w\times L=200\times 1024$. Due to the exact nature of the PDF algorithm, a single realization provides good quality data for $w=200$ tubes. A system length of $L=1024$ is sufficiently long to give the continuum functional form of the profiles. All the data shown below are results of single realization of tubes including the network simulation in the next section. The simulation is stopped before the front exits the system.

1. Density profiles

Figure 6 shows typical particle and tube capacity profiles. There are strong bubble-to-bubble fluctuations and some type of smoothing procedure is necessary. We use the Savitzky-Golay smoothing technique, which approximates successive windows of data points to a fourth order polynomial (solid lines in the figure) [22]. This technique is superior to local averaging because Savitzky-Golay smoothing can faithfully follow rapid changes in the profile, as can be seen in Fig. 6. This smoothing is also useful in estimating the exponents. Since the logarithm of the profile in the tail region amplifies the fluctuation in nonlinear way, the slopes of the raw data in Fig. 8 are larger than those from the smoothed data, and differ from the predicted value of the profile exponent λ.

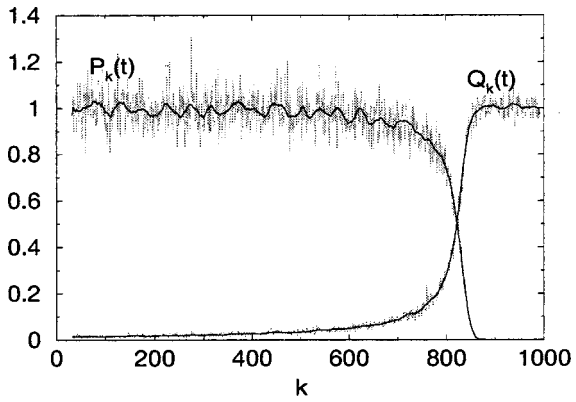

FIG. 6. Normalized profiles for a single realization. Parameters used are $\mu=4$, $\alpha=1$, $\gamma=0.1$, and $\Delta=0.4$. Gray lines are raw data, black lines are smoothed.

2. Front velocity

Figure 7(a) shows the front position, defined as the point where $P_k(t)$ is half of its saturation value, versus time. Notice that a constant front propagation velocity sets in almost immediately. With $\rho=1/\pi$ and $\phi=\pi$, Eq. (27) gives

$$\frac{v}{v_0}=\frac{1}{1+\sqrt{\pi\alpha}/2\Delta}. \qquad (38)$$

The slopes in Fig. 7(a) agree well with Eq. (38). Notice that the propagation velocity does not depend on the reaction strength γ nor the exponent μ in the radius dependence of the velocity.

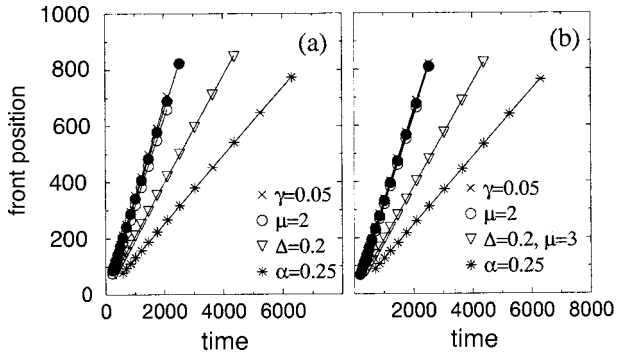

FIG. 7. Front position vs time for different microscopic parameters for (a) the bubble model and (b) the square lattice. Filled circles are for the same parameters as those in Fig. 6. Other data modify these parameters as indicated in the legend. The straight lines are linear fits to the data with slopes of (a) 0.33, 0.32, 0.31, 0.19, 0.12, and (b) 0.32, 0.32, 0.31, 0.19, 0.12, from top to bottom. The corresponding velocities predicted by Eq. (38) are 0.311, 0.311, 0.311, 0.184, and 0.119.

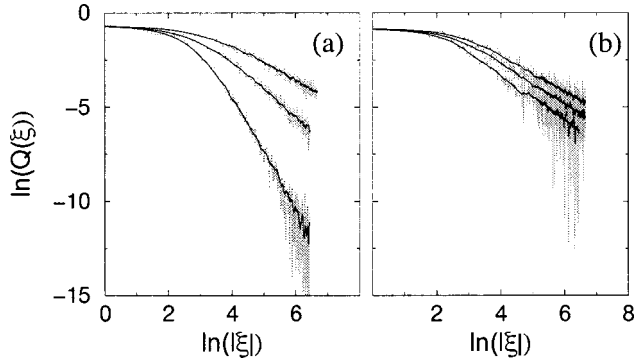

FIG. 8. Tube capacity profile in the tail region on a double logarithmic scale for $\mu=4$, 3, and 2 (top to bottom). Other parameters are the same as in Fig. 6. (a) Bubble model: The slopes of the data in straight region are 0.97 (1), 1.49 (1.5), and 3.17 (3). The numbers in parentheses are the prediction $3/(\mu-1)$. (b) Square lattice: Solid lines are smoothed data. The thick straight lines are linear fits, with slopes 0.95, 1.07, and 1.28.

3. Tail profile

Figure 8(a) shows the tube capacity profile $Q(\xi)$ in the tail region as a function of the distance $|\xi|$ ($\xi<0$) from the front on a double logarithmic scale. The plot becomes straight for large $|\xi|$ and the slope in this region corresponds to the exponent $\lambda=3/(\mu-1)$ predicted by Eq. (37). For the uniform distribution on (0,1), we predicted the profile exponent to be $\lambda=2/(\mu-1)$. For $\mu=4$, the exponent value of 2/3 agrees well with our simulations (Fig. 9). However, for a radius distribution with a lower size cutoff, we expect an exponential density profile (inset to Fig. 9).

As we also discussed in Sec. IV C, the amplitude of the density profile in the tail region typically has a power-law dependence on γ. For a Hertz distribution of particle radii, this amplitude should be proportional to $\gamma^{-\lambda}$ according to Eq. (37). Thus Fig. 10(a) shows $Q(\xi)^{1/\lambda}|\xi|$ versus $1/|\xi|$ for $\mu=4$ and $\mu=3$. Values of the abscissa should be proportional to $1/\gamma$, which is indeed the case.

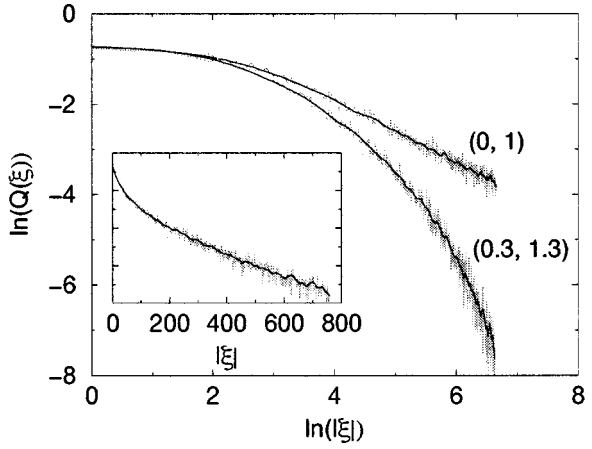

FIG. 9. Tube capacity profile on a double logarithmic scale for a uniform radius distribution on (a,b). Parameters other than the radius distribution are the same as in Fig. 6. The slope of the straight region for $(a,b)=(0,1)$ is 0.63 (predicted value 2/3). Inset: log-normal plot when $(a,b)=(0.3,1.3)$.

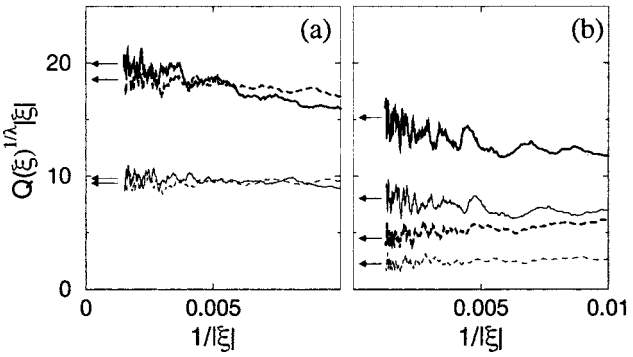

FIG. 10. Dependence of the capacity profile in the tail region on γ. Only smoothed data are shown. Solid curves: $\mu=4$, dashed curves: $\mu=3$. Thick curves: $\gamma=0.05$, thin curves: $\gamma=0.1$. Other parameters are the same as in Fig. 6. (a) Bubble model: The value $\lambda=3/(\mu-1)$ is used. (b) Square lattice: From Fig. 8(b), $\lambda=0.95$ for $\mu=4$ and 1.07 for $\mu=3$ are used. Notice that the abscissa values are proportional to $1/\gamma$ from Eq. (37). Arrows are guides to the eye.

4. Invader profile

Figure 11(a) is a log-normal plot of the invader profile $P(\xi)$ (raw data) versus ξ. The slopes of the two data sets are in excellent agreement with the predicted value $v_0\gamma/(v_0-v)$ from Eq. (32). In the invaded region, since there are few particles present, the corresponding PDF monotonically decreases and its fluctuation is significantly smaller than in the tail region.

V. SQUARE LATTICE NETWORK

We now consider infiltration on a square lattice network of tubes. Here, local mixing at tube junctions occurs as opposed to the mean-field-like mixing in the bubble model. Nevertheless, many of our predictions from the bubble model continue to be valid for the lattice network. For example, we expect that the propagation velocity given by Eq.

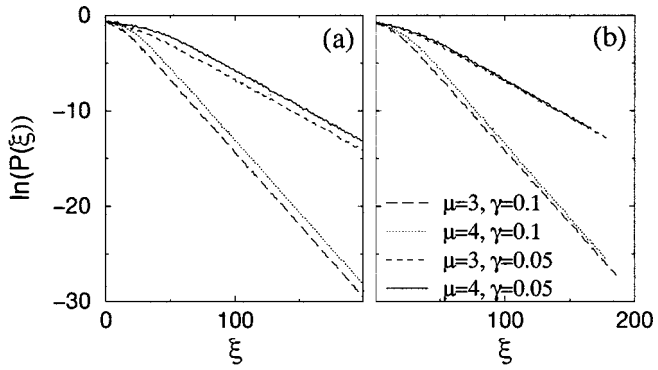

FIG. 11. Log-normal plot of the invaded region. The same data sets as in Fig. 10 are used. The slopes of the straight regions are, from left to right, (a) bubble model: 0.152, 0.150, 0.0744, 0.0748, and (b) square lattice: 0.152, 0.155, 0.0756, 0.0773. The corresponding values of the slope from $v_0\gamma/(v_0-v)$ are 0.145 and 0.0726.

(27) will continue to hold in the lattice network because it is determined *only* by the boundary conditions of the particle flux and initial filter capacity. We also find numerically that the network model has both the same exponential invader profile and the same power-law capacity profile as in the bubble model, although the values of the amplitudes and decay exponents are different. Overall, it appears that the bubble model provides an excellent account of the numerical results from the lattice network.

A. The model

We study a square lattice of size $w \times L = 200 \times 1024$ which is tilted at 45°. A periodic boundary condition is imposed in the transverse direction. The tube radii are drawn from the Hertz distribution of Eq. (17). Notice that the bubble model would arise from this system by merging together all sites at the same longitudinal position. The overall flow rate ϕ is set to π and the particle density to $\rho = 1/\pi$, just as in the bubble model.

For a given set of tube radii, the flow field is calculated by using the conjugate gradient method [22] to solve the set of linear algebraic equations for fluid conservation at each node. The tolerance of the computation is set so that the measured average PDF and the tube capacity in the kth layer are accurate to within 0.01%. After the flow field is solved, we use the same PDF algorithm as in the bubble model to track the motion of the suspended particles. The new features due to the lattice nature of the network are that tubes are only locally connected and that the local flow direction is not always downstream.

B. Numerical results

To facilitate comparisons, all our numerical results for the bubble model and the square lattice are presented side by side. Figure 7 shows the front position versus time for both the bubble model and the square lattice. The square lattice results are in excellent agreement with the bubble model prediction for the front velocity, Eq. (38). Similarly, the tube capacity profile exhibits a power-law tail [Fig. 8(b)]. However, the dependence of the decay exponent λ on μ is much weaker than in the bubble model. As μ decreases from 4 to 2, λ increases slowly from 0.95 to 1.28.

To isolate the dependence of the capacity profile on the trapping probability γ, Fig. 10(b) shows $Q(\xi)^{1/\lambda}|\xi|$ versus $1/|\xi|$ in the tail region. Here, the values of λ used are obtained from Fig. 8(b). Unlike in the bubble model, the overall amplitude has a relatively stronger dependence on μ. However, the dependence on $1/\gamma$ still holds even in the network case. It seems that in the square lattice network μ has more effect on the amplitude of the tail than on the decay exponent.

Lastly, Fig. 11(b) shows the density profile of invaders in the invaded region. The slopes of these particles are almost identical to those of the bubble model. Currently we do not have a clear explanation of this fact. It seems that the network geometry does not affect the profile. In fact, the characteristic decay length, $(v_0 - v)/v_0\gamma$, of the profiles in Fig. 11 is the same as that of the corresponding 1D model in Sec. III B where ρV invaders are injected with velocity v_0 into the chain of defenders of capacity M.

VI. SUMMARY AND DISCUSSION

In this paper, we studied infiltration, in which suspended particles are removed from a carrier fluid as the suspension passes through a porous medium. The trapping mechanism has a built-in saturation so that once all available trapping sites are used up subsequent particles can pass through the medium freely. The particles are assumed to be sufficiently small that their trapping does not change the flow rate. The basic dynamical properties of this infiltration process are the density profile of the invader particles and the capacity profile of the remaining active pores. When the invader profile reaches the end of the system, the output concentration of particles quickly increases to a saturation level and the filter should be discarded. Thus the features of this profile are important in understanding the operating characteristics of infiltration.

We have developed a series of discrete network models to describe the basic characteristics of infiltration, starting with a one-dimensional model and building up to the bubble model, which is a series array of parallel, multiple capacity tubes. The advantage of these quasi-one-dimensional models is that they remain relatively simple, even after incorporating local spatial heterogeneity. The bubble model, in particular, appears to capture many of the quantitative features that we observed in numerical simulations of infiltration on a square lattice tube network. Our modeling is also flexible, so that variations can be easily implemented for case-specific situations.

Our main qualitative result is that basic dynamical features of the system, including the value of the front propagation velocity, the exponential profile of flowing particles in the invaded region, and the power-law capacity profile of pores in the tail region, are relatively insensitive to microscopic details of the model. We have also identified the basic parameters that do affect quantitative features of the profiles. It is useful to summarize these results and to compare with experimental data, as well as with predictions from previous studies based on the reaction-diffusion equation approach [4,6,23].

1. Invader concentration at the output

In typical experiments, the invader concentration at the output is measured as a function of time. A slower propagation velocity shifts this output concentration curve to a later time, as indicated in Fig. 12(a). Typically, the time unit is normalized by the time for passive particles to pass through the system [4,6]. Hence, the amount of the time shift is determined by the ratio v/v_0 rather than by v itself.

A nice set of infiltration experiments, as well as an accompanying numerical study of the reaction-diffusion equation, were performed in [6]. In these experiments, contaminant solutions with different values of the invader particle diameter d but with fixed mass concentration were used. This makes the corresponding number density ρ of invaders in each solution proportional to d^{-3}. Also, since the cross-

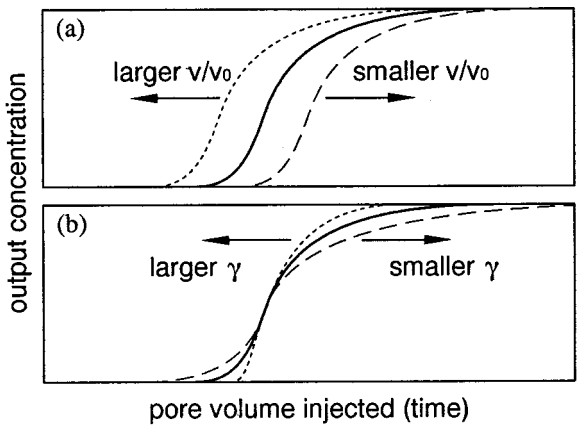

FIG. 12. Qualitative dependence of the output concentration curve (a) on the propagation velocity, and (b) on the reaction strength.

sectional area of each particle is proportional to d^2, the average initial tube capacity M varies as d^{-2}. From Eq. (27), we then have $v/v_0 \sim (1+d)^{-1}$. Thus the output concentration curve shifts to a later time for a solution with a larger value of d, which is consistent with the experiment and numerical predictions in [6].

In another set of experiments, different electrolyte concentrations of the carrier fluid were used. This mainly affects the trapping rate γ. For a larger trapping rate, the width of the output concentration curve, namely, the time range over which the output concentration changes from zero to its saturation value, becomes narrower. However, there is no shift in the breakthrough time because the propagation velocity is independent of γ. These two features are illustrated in Fig. 12(b). This behavior again qualitatively agrees with the experiment in [6].

It would also be interesting to study the effect of different filter grain sizes. In our model this would be accomplished by changing the characteristic parameter α of the pore size distribution. In turn, this affects the invader propagation velocity, and the output concentration curve will shift in time accordingly. However, since the microscopic parameters we use in our modeling may be coupled with each other in experimental situations, different sizes of filter grains or invader particles may also affect, e.g., the reaction strength γ. We can incorporate such a coupling effect by extending our model to deal with these effects explicitly. For example, we can adapt the microscopic models of particle trapping on a single sphere or on a plane [2,8] to the tube geometry. From such an approach, we can express the reaction strength γ as a function of the invader or defender diameter.

2. Tail of the output concentration curve

A slowly decaying tail in the deviation of the output concentration from its asymptotic value is generally observed in experiments [4,6,23]. This observation is in contrast to the empirical approaches, such as that given in [6], which give an exponential profile for the whole time range. Their prediction agrees with experimental observations at early times but then deviates at later times, implying that the output profile at later times is not exponential.

A closely related approach, based on the study of a reaction-diffusion equation, is presented in [4], along with experiments that measure the output concentration. Unlike in [6], here the adsorption rate depends on the local concentration of contaminants and thus is spatially inhomogeneous. A crossover from a rapid increase to a slowly decaying tail of the output concentration was numerically predicted. However, the functional forms of these two regimes—in particular, whether they are exponential or power law in time—were not investigated quantitatively. Nevertheless, the data presented in this work seem consistent with a slower than exponential decay of the density profile.

In [23], an exponential output concentration profile $c(x) \sim \exp(-\Lambda x)$ is assumed from the outset, where x is the downstream distance and Λ is the experimentally measured filter coefficient. The corresponding experimental data show that Λ is constant at early times, and then sharply decreases at later times. Thus the initial stage of the experiment is consistent with an exponential profile, but later the profile decays more slowly. In [23], this is attributed to a "blocking effect" in which previously deposited particles can block the further deposition of particles onto nearby available trapping sites.

3. Probability of encountering an open trap

As a last remark, let us examine the assumption that the probability of encountering an open trap is proportional to the fraction of open traps in a pore (Sec. III B). Suppose instead that one takes into account the volumetric effect that particles far from the surface of the pore do not have the chance to encounter a trap. Then the fraction of particles in contact with the inner surface of a tube is proportional to $1/r$, namely, the ratio between the surface area and the volume of the tube. This would lead to the interaction terms involving T_k in Eqs. (25) and (26) being multiplied by another factor of $1/r$. However, this modification does not affect the propagation velocity of the front, nor the power-law feature of the tail. Only the decay exponent changes through the steps of Eqs. (33)–(36) with an additional factor of $1/r$.

Our results can also provide practical guidelines for improving the design of a filter in two aspects, namely, the breakthrough time and the amount of filter material used before the breakthrough. A longer breakthrough time can be achieved by having a smaller filter grain size, a lower input concentration, or a larger pore capacity. While these trends may seem intuitively clear, we can quantitatively estimate the increase in the breakthrough time through the expression for the propagation velocity, Eq. (27). When breakthrough occurs, the amount of unused filter material is determined by the shape of the tail in the density profile of the defenders. According to Eq. (37), the amplitude of this tail is proportional to $\gamma^{-\lambda}$. From this, we can quantitatively estimate the amount of filter material left unused at the breakthrough time as a function of the reaction strength.

ACKNOWLEDGMENTS

We thank Dr. Jysoo Lee for helpful discussions about flow field calculations. We are also grateful to ARO Grant

No. DAAD19-99-1-0173 and NSF Grant No. DMR9978902 for financial support.

APPENDIX: SOLUTION OF THE HYDRODYNAMIC DISPERSION EQUATION

We solve the master equations Eq. (19) by the Laplace transform method. Define $\tilde{p}_k(s) \equiv \int_0^\infty dt\, p_k(t) e^{-st}$ and take the Laplace transform of Eq. (19) to find

$$s\tilde{p}_0 = \frac{\rho\phi}{s} - \frac{\tilde{p}_0}{\tau_0}, \quad s\tilde{p}_k = \frac{\tilde{p}_{k-1}}{\tau_{k-1}} - \frac{\tilde{p}_k}{\tau_k}. \tag{A1}$$

Rearranging yields

$$\frac{\tilde{p}_0}{\tau_0}(1+\tau_0 s) = \frac{\rho\phi}{s}, \quad \frac{\tilde{p}_k}{\tau_k}(1+\tau_k s) = \frac{\tilde{p}_{k-1}}{\tau_{k-1}}. \tag{A2}$$

We multiply the above equations for indices $0,1,2,\ldots,k$ together and rearrange terms yet again to obtain

$$\frac{\tilde{p}_k}{\tau_k} \prod_{m=0}^{k} (1+\tau_m s) = \frac{\rho\phi}{s}. \tag{A3}$$

Before taking averages, we use $\tau_k = (1/s)[1 - 1/(1+\tau_k s)](1+\tau_k s)$ on the left hand side of Eq. (A3) to get

$$\tilde{p}_k \prod_{m=0}^{k} (1+\tau_m s) = \frac{\rho\phi}{s^2}\left(1 - \frac{1}{1+\tau_k s}\right)(1+\tau_k s). \tag{A4}$$

Averaging over the residence time distribution $R(\tau)$ defined by Eq. (20), we obtain

$$\langle \tilde{p}_k \rangle = \frac{\rho\phi}{s^2}(1-B)B^k, \quad B \equiv \left\langle \frac{1}{1+\tau s} \right\rangle, \tag{A5}$$

where $\langle \cdot \rangle$ denotes an average over $R(\tau)$. Note that B does not depend on m because all the τ_m's are independent and identically distributed in the large w limit. For the long time limit, we need the small s behavior of B. Accordingly, we expand $B = 1 - s\langle\tau\rangle + s^2\langle\tau^2\rangle \cdots$ in terms of the moments $\langle \tau^m \rangle$.

The profile of the carrier fluid (dashed line in Fig. 2) is monotonically decreasing near the front, and thus can be characterized by its first derivative, which gives a bell shaped distribution centered at the front. We divide the derivative by the total sum of derivatives $\Sigma_m(\langle p_m\rangle - \langle p_{m-1}\rangle) = -\langle p_0\rangle$ to obtain the normalized probability distribution of the front,

$$\mathcal{P}(k) = \frac{1}{\langle p_0\rangle}[\langle p_{k-1}\rangle - \langle p_k\rangle]. \tag{A6}$$

The average position of the front is, using Eq. (A5) and the steady state solution of Eq. (19), $\langle p_0\rangle = \rho\phi\langle\tau\rangle$,

$$\begin{aligned}
\langle \bar{k} \rangle &= \frac{1}{\langle p_0\rangle} \sum_k k[\langle p_{k-1}\rangle - \langle p_k\rangle] \\
&= \frac{1}{\langle p_0\rangle} \mathcal{L}^{-1}\left(\sum_k k[\langle \tilde{p}_{k-1}\rangle - \langle \tilde{p}_k\rangle] \right) \\
&= \frac{1}{\langle \tau\rangle} \mathcal{L}^{-1}\left(\frac{1-B}{s^2} \sum_k k[B^{k-1} - B^k] \right) \\
&\simeq \frac{t}{\langle\tau\rangle},
\end{aligned} \tag{A7}$$

where the overbar means averaging over $\mathcal{P}(k)$, and $\mathcal{L}^{-1}$ is the inverse Laplace transform. We use the identity $\mathcal{L}^{-1}(s^{-\beta}) = t^{\beta-1}/\Gamma(\beta)$ for the last step. We assume a sufficiently long chain of bubbles in the summations above to prevent a finite length effect. From above, we find the propagation velocity as $v = \langle\tau\rangle^{-1}$ [Eq. (23)].

Similarly, $\langle \bar{k}^2 \rangle = \langle p_0\rangle^{-1} \Sigma_k k^2 [\langle p_{k-1}\rangle - \langle p_k\rangle]$, and the width of the front is

$$[\langle \bar{k}^2\rangle - \langle \bar{k}\rangle^2]^{1/2} \simeq \left\{ \frac{t}{\langle\tau\rangle}\left[2\Gamma\left(1+\frac{\mu}{2}\right)\Gamma\left(3-\frac{\mu}{2}\right) - 1 \right] \right\}^{1/2}, \tag{A8}$$

which gives Eq. (24).

[1] C. Tien and A. C. Payatakes, AIChE J. **25**, 737 (1979).
[2] R. F. Probstein, *Physicochemical Hydrodynamics*, 2nd ed. (John Wiley & Sons, New York, 1994).
[3] A. O. Imdakm and M. Sahimi, Phys. Rev. A **36**, 5304 (1987).
[4] L. Lührmann, U. Noseck, and C. Tix, Water Resour. Res. **34**, 421 (1998).
[5] L. Bloomfield, Sci. Am. **281**, 152 (1999).
[6] D. Putnam and M. Burns, Chem. Eng. Sci. **52**, 93 (1997).
[7] H. Brenner and D. A. Edwards, *Macrotransport Processes* (Butterworth-Heinemann, Stoneham, MA, 1993).
[8] R. Rajagopalan and C. Tien, AIChE J. **22**, 523 (1976).
[9] J. Lee and J. Koplik, Phys. Rev. E **54**, 4011 (1996).
[10] C. Ghidaglia, L. de Arcangelis, J. Hinch, and E. Guazzelli, Phys. Rev. E **53**, R3028 (1996).
[11] S. Datta and S. Redner, Phys. Rev. E **58**, R1203 (1998); Int. J. Mod. Phys. C **9**, 1535 (1998).
[12] A. O. Imdakm and M. Sahimi, Chem. Eng. Sci. **46**, 1977 (1991).
[13] S. Rege and H. Fogler, Chem. Eng. Sci. **42**, 1553 (1987).
[14] H. Chiang and C. Tien, AIChE J. **31**, 1349 (1985).
[15] V. G. Levich, *Physicochemical Hydrodynamics* (Prentice-Hall, Englewood Cliffs, NJ, 1962).
[16] H. E. Daniels, Proc. R. Soc. London, Ser. A **183**, 404 (1945); D. G. Harlow and S. L. Phoenix, J. Compos. Mater. **12**, 195 (1978); S. L. Phoenix and R. L. Smith, J. Appl. Mech. **103**, 75 (1981); D. Sornette and S. Redner, J. Phys. A **22**, L619 (1989); P. L. Leath and P. M. Duxbury, Phys. Rev. B **49**, 14 905 (1994).

[17] B. Kahng, G. G. Batrouni, and S. Redner, J. Phys. A **20**, L827 (1987).
[18] G. H. Thomas, G. R. Countryman, and I. Fatt, Soc. Pet. Eng. J. **3**, 189 (1963); I. Chatzis and F. A. L. Dullien, Int. Chem. Eng. **25**, 47 (1985).
[19] J. Koplik, S. Redner, and E. J. Hinch, Phys. Rev. E **50**, 4650 (1994).
[20] L. Niemeyer, L. Pietronero, and H. J. Wiesmann, Phys. Rev. Lett. **52**, 1033 (1984); S. Havlin, M. Dishon, J. E. Kiefer, and G. H. Weiss, *ibid.* **53**, 407 (1984).
[21] W. Hwang, Ph.D. thesis, Boston University, 2001.
[22] W. H. Press, S. A. Teukolsky, W. T. Vetterling, and B. P. Flannery, *Numerical Recipes in C*, 2nd ed. (Cambridge University Press, Cambridge, 1999).
[23] R. Vaidyanathan and C. Tien, Chem. Eng. Sci. **46**, 967 (1991).